

Journal Pre-proof

Georectifying drone image data over water surfaces without fixed ground control: methodology, uncertainty assessment and application over an estuarine environment

Jennifer Watts, Thomas Holding, Karen Anderson, Thomas G. Bell, Bertrand Chapron, Craig Donlon, Fabrice Collard, Neill Wood, David Walker, Leon DeBell, James P. Duffy, Jamie Shutler

PII: S0272-7714(24)00241-5

DOI: <https://doi.org/10.1016/j.ecss.2024.108853>

Reference: YECSS 108853

To appear in: *Estuarine, Coastal and Shelf Science*

Received Date: 1 May 2023

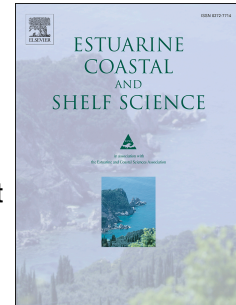
Revised Date: 14 June 2024

Accepted Date: 19 June 2024

Please cite this article as: Watts, J., Holding, T., Anderson, K., Bell, T.G., Chapron, B., Donlon, C., Collard, F., Wood, N., Walker, D., DeBell, L., Duffy, J.P., Shutler, J., Georectifying drone image data over water surfaces without fixed ground control: methodology, uncertainty assessment and application over an estuarine environment, *Estuarine, Coastal and Shelf Science*, <https://doi.org/10.1016/j.ecss.2024.108853>.

This is a PDF file of an article that has undergone enhancements after acceptance, such as the addition of a cover page and metadata, and formatting for readability, but it is not yet the definitive version of record. This version will undergo additional copyediting, typesetting and review before it is published in its final form, but we are providing this version to give early visibility of the article. Please note that, during the production process, errors may be discovered which could affect the content, and all legal disclaimers that apply to the journal pertain.

© 2024 Published by Elsevier Ltd.



Georectifying drone image data over water surfaces without fixed ground control: methodology, uncertainty assessment and application over an estuarine environment

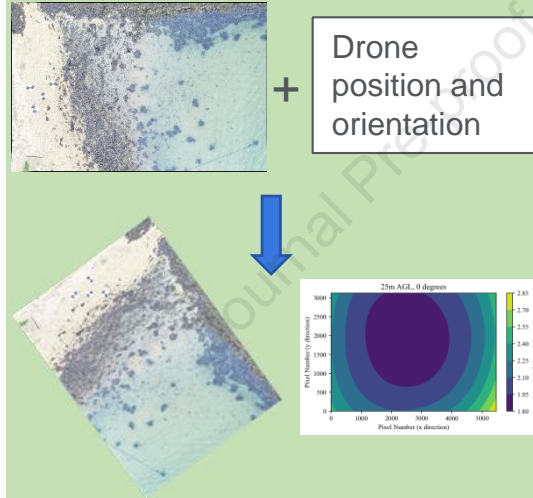
Issue and solution

To produce **spatially correct** data using drones requires images to be **georectified**

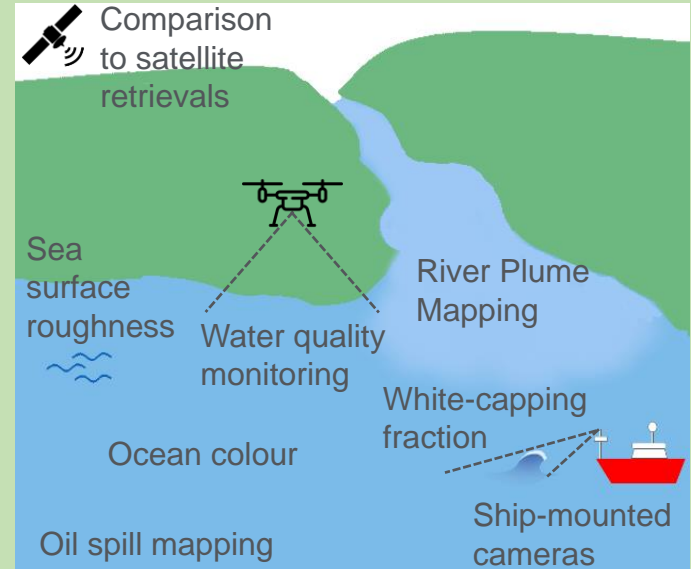
To make observations of the water surface using drones, methods are needed which do not rely on fixed points of reference

We present a simple to use automated workflow for georectifying individual aerial images using position and orientation data from the drone's on-board sensors.

Example



Potential Applications



1 **Georectifying drone image data over water surfaces without fixed**
2 **ground control: methodology, uncertainty assessment and application**
3 **over an estuarine environment**

4 **Jennifer Watts^{1*}, Thomas Holding², Karen Anderson³, Thomas G. Bell⁴, Bertrand Chapron⁵,**
5 **Craig Donlon⁶, Fabrice Collard⁷, Neill Wood⁸, David Walker⁹, Leon DeBell¹⁰, James P. Duffy¹¹,**
6 **Jamie Shutler¹**

7 ¹Centre for Geography and Environmental Science, University of Exeter, Penryn, Cornwall, UK.

8 ²Max Planck Institute for Evolutionary Anthropology, Deutscher Platz 6, 04103 Leipzig

9 ³Environment and Sustainability Institute, University of Exeter, Penryn, Cornwall

10 ⁴Plymouth Marine Laboratory, Plymouth, Devon, UK.

11 ⁵Univ. Brest, CNRS, IRD, Ifremer, Laboratoire d'Océanographie Physique et Spatiale, IUEM, 29280,
12 Brest, France

13 ⁶ ESTEC, European Space Agency, The Netherlands.

14 ⁷OCEAN DATA LAB, Brest, France

15 ⁸Camborne School of Mines, University of Exeter, Tremough Campus, Penryn TR10 9EZ

16 ⁹Paddle Logger Limited, Office 1 The Warehouse, Anchor Quay, Falmouth, Cornwall, United
17 Kingdom, TR10 8GZ

18 ¹⁰Somerset Environmental Records Centre, Somerset Wildlife Trust, 34 Wellington Road, Taunton
19 TA1 5AW

20 ¹¹DEFRA, Seacole Building, 2 Marsham St, London SW1P 4DF

21 *Corresponding author: Jennifer Watts (j.h.watts@exeter.ac.uk)

22

23

Abstract

24 Light-weight consumer-grade drones have the potential to provide geospatial image data to study a
25 broad range of oceanic processes. However, rigorously tested methodologies to effectively and
26 accurately geolocate and rectify these image data over mobile and dynamic water surfaces, where
27 temporally fixed points of reference are unlikely to exist, are limited. We present a simple to use
28 automated workflow for georectifying individual aerial images using position and orientation data
29 from the drone's on-board sensor (i.e. direct-georectification). The presented methodology includes
30 correcting for camera lens distortion and viewing angle and exploits standard mathematics and camera
31 data processing techniques. The method is used to georectify image datasets from test flights with
32 different combinations of altitude and camera angle. Using a test site over land, directly-georectified
33 images, as well as the same images georectified using standard photogrammetry software, are
34 evaluated using a network of known ground control points. The novel methodology performs well
35 with the camera at nadir (both 10 m and 25 metres above ground level) and exhibits a mean spatial
36 accuracy of ± 1 metre. The same accuracy is achieved when the camera angle is 30° at 10 metres
37 above ground level but decreases to ± 2.9 metres at 30° and 25 metres. The accuracy changes because
38 the uncertainties are a function of the altitude and angle of the camera versus the ground. Drone in-
39 flight positioning errors can reduce the accuracy further to ± 5 metres with the camera at 30° and 25
40 metres. An ensemble approach is used to map the uncertainties within the camera field-of-view to
41 show how they change with viewing distance and drone position and orientation. The complete
42 approach is demonstrated over an estuarine environment that includes the shoreline and open water,
43 producing results consistent with the land-based field-tests of accuracy. Overall, the workflow
44 presented here provides a low cost and agile solution for direct-georectification of drone-captured
45 image data over water surfaces. This approach could be used for collecting and processing image data
46 from drones or ship-mounted cameras to provide observations of ocean colour, sea-ice, ocean glitter,
47 sea surface roughness, white-cap coverage, coastal water quality, and river plumes. The Python scripts
48 for the complete image georectification workflow, including uncertainty map generation, are available
49 from <https://github.com/JamieLab/SArONG>.

50 1 Introduction

51 Light-weight consumer-grade drones are an agile and cost-effective tool for capturing low-
52 altitude (< 120 m) images and fine spatial resolution geospatial information. The spatial and temporal
53 resolution (e.g. 10 mm per pixel, sub-hourly) of data collected by drones can effectively bridge the
54 gap between satellite datasets (m to km, daily to monthly) and discrete *in situ* measurements. As a
55 result, drones have shown considerable promise for a range of scientific studies. In marine and coastal
56 science, the applications and uses of drone technology are diverse and include coastal management
57 (e.g. Duffy et al., 2018; Pucino et al., 2021), conservation (Johnston, 2019), ecology (e.g. Ventura et
58 al., 2018) and biological oceanography (e.g. Gray et al., 2022).

59 To create high-quality geospatial datasets from drone image datasets, such as orthomosaics
60 from overlapping sets of imaging data, the data first needs to be georectified. Georectification is the
61 process by which images are corrected for spatial variations caused by the camera lens and differences
62 in viewing angle between the drone and Earth's surface and then projected into a known coordinate
63 system. Over terrestrial systems it is possible to generate orthomosaics without the use of measured
64 ground control points using just the Exchangeable Image File Format (EXIF) or Extreme memory
65 Profile (XMP) tagged images often captured by drones. These image tags typically contain
66 information on the intrinsic camera parameters (e.g. focal length) as well as the camera position and
67 orientation at the time of image capture. Computer-vision based photogrammetry software uses this
68 information in conjunction with static tie-points that are visible from multiple images or viewpoints
69 (identifiable points of interest such as points of high contrast or interesting texture) for
70 georectification. These tie-points and image tags can be used as input to structure-from-motion
71 techniques which estimate the 3D position of these static tie-points in space by triangulating their
72 locations from multiple images. The 3D model produced by structure-from-motion can then be further
73 refined using bundle adjustment algorithms, which refine the tie-point matching to produce an optimal
74 3D construction based on minimising re-projection errors. For higher accuracy scene reconstruction,
75 easily discernible fixed points of reference within the camera field-of-view, such as permanent or
76 static features or deliberately placed ground control points (GCPs) are used. These fixed positions –
77 often surveyed using differential Global Navigation Satellite System (GNSS) real-time-kinematic

78 (RTK) equipment –provide consistent points of reference in real-world coordinates allowing image
79 mosaics to be constructed and evaluated. Positional accuracy without the use of GCPs can be
80 improved using real-time-kinematic drone systems; however, these require connection to a base
81 station (a stationary object with defined precise coordinates), and they are an order of magnitude more
82 expensive to purchase (e.g. thousands of £ compared to hundreds of £) than standard drone imaging
83 equipment without real-time-kinematic capabilities. Connection to a stable base station in marine
84 environments, other than coastal regions near to infrastructure, is generally not possible. Furthermore,
85 even with the use of a real-time-kinematic drone system, the stated accuracy values are not
86 necessarily achieved in the final processed data products (Ekaso et al., 2020). With all of these
87 approaches, it is common for drone collected image datasets to be processed using workflows in
88 photogrammetry software that have been developed for land-based applications and assessment (e.g.
89 Agisoft Metashape, Pix4D), and all rely on the existence of stationary points within the camera field-
90 of-view within all images.

91 It is not possible to identify static tie-points or deploy fixed ground control points to study
92 dynamic or mobile environments such as water surfaces (Jeziorska, 2019). This is due to candidate
93 features (e.g., breaking waves) being short lived and transient in comparison to the image capture
94 speed or drone movements, and so these features are unlikely to exist within multiple camera views,
95 or they will have moved, deformed, or evolved. As a result, quantitative drone studies have been
96 mostly limited to the intertidal zone or other near-coast ecosystems and environments where either
97 tie-points can be identified, or ground control can be deployed. Examples from the literature include
98 using structure-from-motion photogrammetric techniques (Cavanaugh et al., 2021; Cunliffe et al.,
99 2019; Duffy, Pratt, et al., 2018), image co-registration onto a basemap (Mallast & Siebert, 2019) or
100 RTK-enabled drones (Seymour et al., 2018). In these environments, it is still feasible to produce
101 orthomosaics by using feature-matching techniques between overlapping images (e.g. the coastline or
102 features on the sea-bed). In contrast, studies using drones in offshore environments have mostly
103 focused on applications where accurate georectification of image datasets is not necessary, such as
104 observing and counting marine mega fauna (Williamson et al., 2021, see the references within:
105 Johnston, 2019; Kislik et al., 2018) or identification of floating macro-litter (Andriolo et al., 2022). In

106 these examples, if a specific geolocation position is required for a target within the image view the
107 drone position itself (longitude and latitude) is used without considering the true sensor field-of-view
108 or orientation. Other studies have used this approach to geolocate sea-surface observations from
109 alternative (non-imaging) drone-mounted sensors, for example infrared thermometers (Cassano et al.,
110 2016) and hyperspectral radiometers (Shang et al., 2017). Geolocating data in this way assumes that
111 the sensor remained at nadir (i.e. its orientation was unaffected by the movement of the drone or that
112 the drone was horizontally and vertically stable during data collection). Please see Text S1 in the
113 supporting information for a detailed description of the methods used in published marine studies to
114 georectify image data over water surfaces without ground control.

115 If information on the camera specifications, position, and orientation (as required to
116 determine its field-of-view) are known then individual images collected by drones can be directly
117 georectified. This technique has been widely used in terrestrial applications, however there are limited
118 instances in the literature where images collected by drones over solely water surfaces have been
119 processed using direct-georectification. Examples include the use of video-stream image mosaicking
120 techniques developed for over land (Zhou, 2010) to make observations of the sea surface (Zappa et
121 al., 2020) and direct-georectification of individual images for the extraction of sea surface state
122 (Almar et al., 2021). However, in both studies there is limited evidence of a rigorous assessment of
123 the accuracy and precision of the georectification procedure used, its appropriateness for use over a
124 dynamic water environment or its resultant impact on any extracted datasets.

125 The spatial accuracy of images that have undergone direct-georectification is a function of the
126 accuracy of the interior orientation parameters (e.g. camera lens distortion) and the accuracy of the
127 exterior orientation parameters recorded by the drone on-board sensors (easting, northing, altitude)
128 and camera and drone orientation (roll, pitch, yaw). There is a tendency for studies to characterise
129 data uncertainty according to the equipment's manufacturer reported maximum accuracy values (e.g.
130 Zappa et al., 2020) as these are readily available or no more specific information exists. However, in
131 practice, it is unlikely that maximum positioning values are achievable during all field operations and
132 conditions (Schweitzer & Cowen, 2022). Characterising uncertainties and their impact on final image

133 georectification accuracy is an essential step towards enabling drone-collected datasets to be used
134 more widely for offshore marine applications.

135 We present and evaluate an open-source workflow for georectifying individual low-altitude
136 consumer-grade drone images using the camera specifications and the on-board positional and
137 orientation information recorded by the drone internal sensors. This work is limited to single image
138 georectification as the target environments are mobile water surfaces, meaning conditions can vary at
139 frequencies higher than the image sampling within a drone survey.

140 The aim of this work is to address the following research questions:

- 141 (1) Can drone image data be georectified using only on-board positional and orientation
142 information without the use of ground control or image tie points?
- 143 (2) What is the accuracy of individual image georectification without ground control points and
144 how does this vary with changing flight parameters (e.g. altitude and camera angle)?
- 145 (3) How does the performance of on-board sensors recording drone position (GNSS coordinates,
146 altitude) and orientation (roll, pitch, yaw) vary and what is the impact on image
147 georectification accuracy and precision?

148 2 Methods

149 The methods presented here comprise a description of two uses of a direct-georectification
150 workflow that has been implemented within Python. The first use is for a field experiment designed to
151 enable assessment of the method uncertainties and the second is to collect image data over an example
152 estuarine environment. Sections 2.1 to 2.3 describe the uncertainty assessment field experiment set-up
153 and data collection while section 2.4 describes the direct-georectification workflow itself. Sections 2.5
154 and 2.8 then cover the uncertainty assessment data analysis while section 2.9 describes the collection
155 and analysis of optical image data over an estuarine environment.

156 2.1 Field site and ground survey

157 On land field-tests were conducted at a site in Blackwater, Cornwall, UK (50.280 °N, 5.153
158 °W). These land-based field tests enabled the direct-georectification workflow (used to georectify the
159 images) to be evaluated against a network of measured ground control points, and the same images

160 were georectified using standard photogrammetry software (Agisoft Metashape, both with and
161 without the use of fixed ground control points). Collectively this allows the direct-georectification
162 method to be evaluated and placed into the context of the results from standard land-focussed
163 georectification methods. The site is low-relief area of grass with an average elevation of 133.7 ± 1
164 metres and a slope of 5 % as can be seen on the digital surface models shown on Figures 1a and 1b.
165 The site is exposed to broken and turbulent wind-fields due to trees and building structures along its
166 perimeter with heights up to and over 25 metres above ground level.

167 A grid of ground control points (GCPs) ($n = 59$) with 5 metre spacing was installed using
168 black and white grid targets (Figure 1). The GCPs used in this work consisted of a mixture of sewn or
169 spray painted chequered black and white fabric targets (300 x 300 mm in size). Each GCP was
170 secured to the ground on all four corners using metal pegs. The easting (m), northing (m) and
171 elevation (m) of the centre of each target was measured using a differential GNSS (D-GNSS) RTK
172 Leica GS-08 plus survey system (manufacturer stated accuracy of ~ 5 mm horizontally and ~ 10 mm
173 vertically). The D-GNSS RTK system consisted of a base station, set up over a static control point
174 installed at the field site (see Figure 1) and a rover kit used to take the measurements.

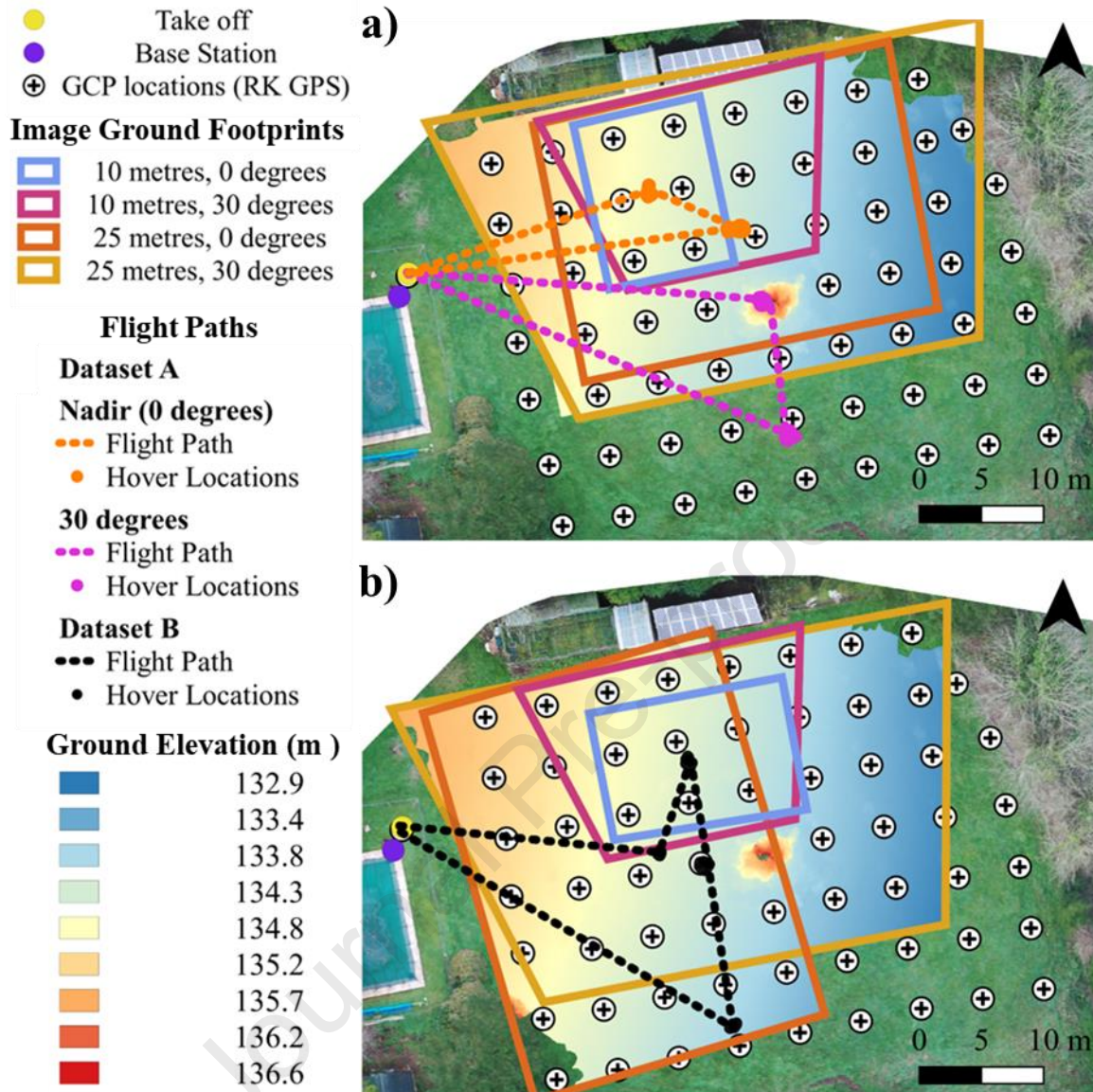


Figure 1. The field-site and GCP set-up, location of the D-GNSS RTK base station (purple) drone take off point (yellow) and the image ground footprints for each altitude and camera angle for Dataset A (Figure 1a, top panel) with flight paths and hover locations shown in orange (nadir) and pink (30°) and Dataset B (Figure 1b, bottom panel) with flight paths and hover flight locations shown in black. The black and white symbols show the positions of the D-GNSS RTK measured GCP targets. Also shown is the image field-of-view specific digital surface model of site topography. These data were produced by Agisoft Metashape from a gridded aerial survey and the D-GNSS RTK measured GCP targets.

175 2.2 Drone platform and sensor equipment

176 Images were collected using a DJI Mavic 2 Pro (DJI M2P) with an in-built Hasselblad camera
177 (Horizontal field-of-view of 64.94° , Vertical field-of-view of 51.03°). Each DJI M2P image is $5472 \times$
178 3648 pixels. The DJI M2P records positional data in World Geodetic System 1984, WGS-84, as
179 longitude, latitude and elevation using a single GNSS unit containing a GNSS chip (type UBX-
180 M8030) enabled to receive both the Global Positioning System (GPS) and Global Navigation Satellite
181 System (GLONASS) networks. The drone measures altitude above take-off point (metres) using a
182 barometric sensor and altitude above ground level (metres) at the drone position using a sonar sensor.
183 The drone measures yaw (compass heading in degrees) using a single magnetic internal compass
184 module and pitch (in degrees) and roll (in degrees) using a pair of inertial motion units (IMUs).
185 Manufacturer specifications for the accuracy of the DJI Mavic 2 Pro sensors is unavailable as it is
186 proprietary information.

187 2.3 Airborne surveys

188 Sets of images were collected over the grid of GCPs by maintaining the drone in a fixed
189 position (hovering) at an altitude of 10 m and 25 m above ground level with the camera at an angle of
190 0° (nadir) and 30° from nadir in the forward direction (relative to the drone platform). Example
191 ground footprints for each hover flight are shown on Figure 1. These images had a resultant areal
192 footprint of 120 m^2 (10 m, 0°), 389 m^2 (10 metres, 30°), 768 m^2 (25 metres, 0°) and 1352 m^2 (25
193 metres, 30°). Image collection was undertaken using hover flights in order to collect multiple images
194 with stable position and orientation information from the drone sensors. The collection of these sets of
195 images (instead of single images) enables statistical assessment of the time-varying performance of
196 the drone on-board sensor. Flights were made manually with the drone in GPS mode (P-mode).
197 During each flight, the hover position for each altitude and camera angle combination was selected
198 manually to provide the best within-image coverage of ground control points using the camera field-
199 of-view livestream displayed on the ground station controller. See Figure 1 for flight path information
200 and hover points and supporting information Table S1 for further details of these two datasets. For
201 each combination of altitude and camera angle (a total of $n = 4$), the drone maintained its position
202 over the grid of ground control points for two minutes (using the inbuilt hover capability) and

203 captured images every 2 seconds using the auto-timer capture function. This resulted in four aerial
204 image sets, one for each altitude and camera angle combination, consisting of ~60 overlapping
205 images. This was repeated to produce Dataset A and Dataset B which were collected over different
206 days (see Table S1, supporting materials). Collecting data on different days allowed the impact of
207 differing environmental conditions (e.g. wind conditions) to be examined (see supporting materials,
208 Figure S4.1, Text S4.4) or effects due to time-varying sensor accuracy to be observed (see discussion
209 in section 4.4.2).

210 2.4 Direct-georectification in Python

211 The workflow for the direct georectification method is given in Figure 2 and the critical steps
212 which comprise the georectification process are the lens distortion correction and the image
213 reprojection, which includes the image corner calculation step. Other aspects of this description are
214 specific to the platform used within this work and thus could be adapted for other sensor and drone set
215 ups. The full Python implementation is freely available from <https://github.com/JamieLab/SArONG>.
216 This workflow was implemented in Python version 3.6 and executed on an HP Elitebook with an Intel
217 Core i5-10310U central processing unit (standard based frequency of 1.7 GHz), running a 64-bit
218 operating system with 16.0 GB of memory. Georectification of a single image takes ~ 6 seconds. The
219 following methods describe each of the steps given in Figure 2.

220 2.4.1 Lens Distortion Correction

221 Images are corrected for lens distortion using camera calibration tools in the open-source
222 computer vision and machine learning software library OpenCV (version 3.4.2). Prior to use on the
223 drone, OpenCV was used to calculate lens distortion coefficients from a set of calibration images ($n =$
224 20) of a 9 by 6 chessboard pattern taken using the drone camera at varying distances and angles. The
225 lens distortion coefficients for the DJI M2P can be viewed in the `camera_calibration_settings.py`
226 script within the linked GitHub repository. The resultant lens distortion coefficients are applied to
227 each image using a custom Python script (`calibrate.py`), the basis of which is bundled with OpenCV,
228 whereas this has been edited to stop the removal of edge data. The workflow automatically saves all

229 corrected images in a separate file without altering the image format (e.g. .jpg, .raw). In this work
 230 .raw image files were used to avoid compression artefacts.

231

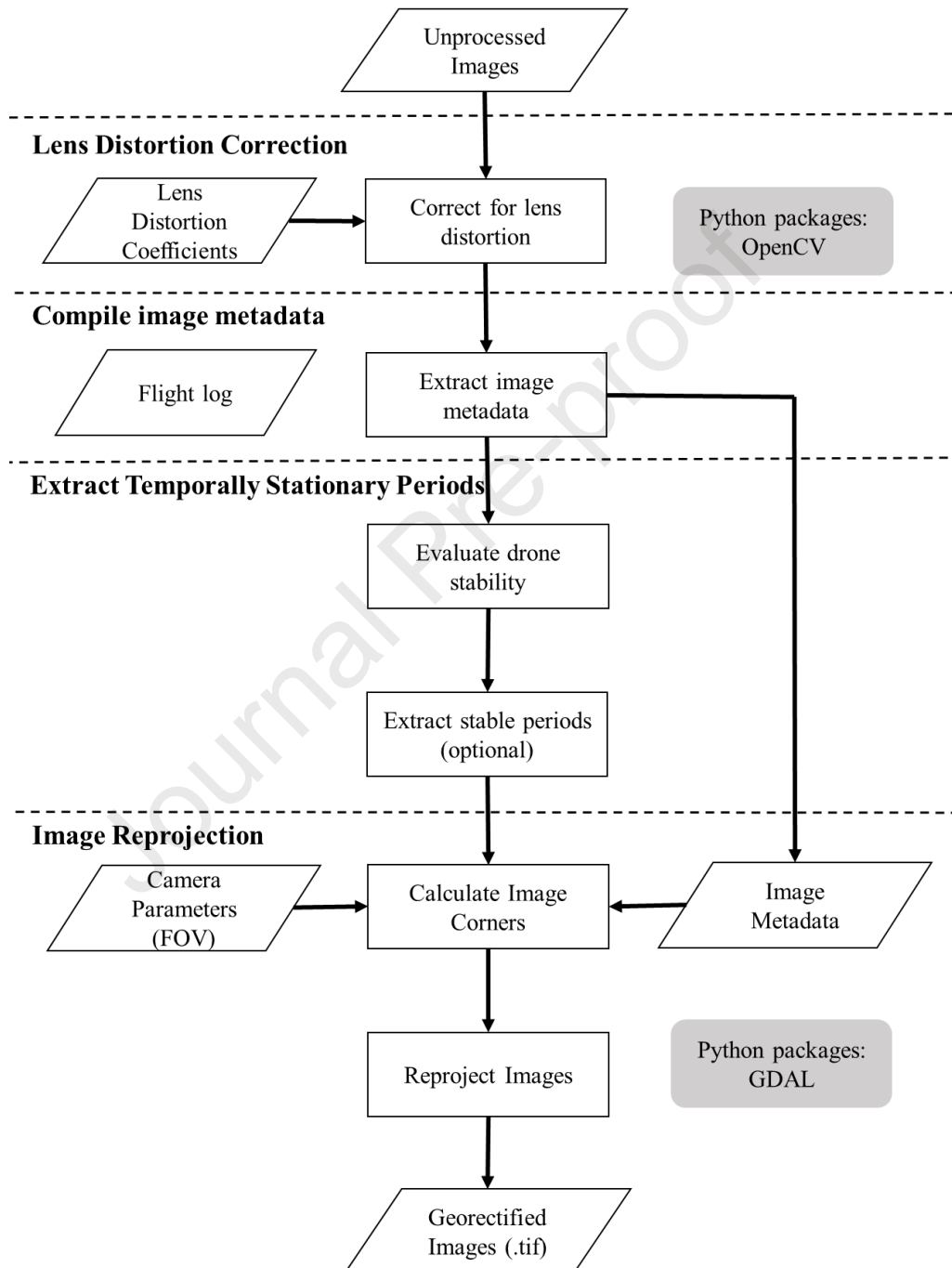


Figure 2. Image processing workflow for the Python direct-georectification methodology

232 2.4.2 Extracting image metadata

233 The DJI M2P automatically geotags each image in the EXIF header with the camera
234 longitude, latitude, and elevation above the ellipsoid (in WGS84). Flight logs (logged at a frequency
235 of 10 Hz) containing additional information on drone position (altitude above ground level in m) and
236 orientation data (roll, pitch, yaw) were extracted in .csv format using AirData UAV
237 (<https://airdata.com>). AirData UAV (HD Free Version) is a free software that processes the encrypted
238 flight data created by DJI compatible flight control apps used to initiate the DJI M2P flights (e.g. DJI
239 GO4).

240 The AirData UAV flight logs contain information on the DJI M2P image capture times
241 collocated with flight parameters. Using this information, an image-wise metadata file (.csv) is
242 created which lists the undistorted image file name alongside the drone position (longitude, latitude,
243 and elevation (WGS84), easting and northing (British National Grid), altitude above ground level at
244 the drone position (metres), altitude above ground level at drone take off position (metres) and drone
245 orientation (roll, pitch, yaw in degrees). Also recorded is the number of satellites being used for
246 positioning when each image is captured. The AirData UAV flight logs only contain information on
247 the image capture times when the sensor is in-built (e.g. attached to the drone central processing unit).
248 For externally mounted sensors, the Python workflow script can be used instead to extract image
249 metadata and co-locate it with the flight sensor data.

250 2.4.3 Extract stationary periods (optional)

251 This step was not implemented during this work, however an option to filter the data to
252 temporally stationary periods with respect to drone position and camera orientation is included within
253 the Python workflow. The identification of images from these ‘stationary’ periods reduces the effect
254 of any time lag between sensors and changes in position and orientation due to unexpected drone
255 motion. Stationary points are flagged using a rolling standard deviation of each positional parameter
256 over a 20-second window that is then compared to a user-determined threshold. The thresholds for
257 each parameter should be determined experimentally as it is dependent on the platform stability and
258 environmental conditions (e.g. wind-speeds, satellite constellation). However, for a drone platform

259 used in this work we recommend a starting point of 0.00002° for latitude and longitude (which
260 equates to ~ 2 m at the equator), and 2 metres for altitude and 2° for roll, pitch, and yaw. These
261 thresholds can be reduced or increased by examining the resultant filtered image datasets. When the
262 standard deviation is below the chosen threshold the drone is considered to be near-stationary with
263 respect to the parameter of interest. An image flag (stable or unstable) is created and stored in the
264 image metadata file (.csv).

265 2.4.4 Image corner calculation and image reprojection

266 To perform direct-georectification the ‘on-the-ground’ x,y coordinates for each image corner
267 are required. These are determined using standard mathematical ray tracing techniques (Glassner,
268 1989). For each corner, ray vectors are determined from the sensors horizontal and vertical field-of-
269 view. Each ray is rotated according to the drone orientation (roll, pitch, yaw) and its intersection with
270 the ground (assumed to be a flat plane) the position of which is determined using the drone position
271 (longitude, latitude, and altitude). The full mathematical description of the ray tracing approach used
272 in this work is given in the supporting materials (Equations S1 – S23). The Python code for applying
273 the ray tracing follows a variation of the script camera_calculator.py method from
274 <http://gist.github.com/luipir> (Pirelli, L., 2019).

275 The corner coordinates (which in this work are in British National Grid, metres) are used as
276 control points to re-project the image using gdal.warp (version 2.4.1). The workflow (Figure 2)
277 produces a georectified image file (.tif), the equivalent netCDF file containing all metadata (.nc) and a
278 separate file containing a duplicate of the metadata (.vrt).

279 2.5. Image georectification in Agisoft Metashape

280 To create a reference dataset against which the capability of the presented Python
281 methodology could be compared, each hover flight image set was also processed using Agisoft
282 Metashape Professional 2.0.1 (henceforth referred to as Agisoft Metashape), which is a standard
283 photogrammetric software programme. The Agisoft Metashape workflow corrects for radial distortion
284 during camera calibration using the set of image data and information on the camera lens (focal
285 length, pixel size) to calculate interior orientation parameters (including lens distortion parameters).

286 Distinctive tie-points are identified and used to produce a 3D model using structure-from-motion,
287 bundle adjustment and multi-view stereo algorithms, although the exact method used by Agisoft
288 Metashape is proprietary information. These models, and any extracted orthomosaics, can be given
289 real-world coordinates either using the camera position information from the drone or by manually
290 identifying measured ground control points within images. For this work, image sets were processed
291 using two Agisoft Metashape workflows, one using just the camera position information from the
292 drone (Agisoft Metashape without GCPs) and one using user identified D-GNSS RTK measured
293 GCPs (Agisoft Metashape with GCPs). See supporting information Text S2 and S3 for the details of
294 the Metashape workflows. Individual georectified images can be exported from Agisoft Metashape
295 once an orthomosaic is created, and it is these images that are used in the subsequent analysis.

296 2.6 Georectified image accuracy assessment from all methods

297 The centre of each GCP was visually identified and the position extracted (easting, northing)
298 from the georeferenced images created by all three methodologies (Direct-georectification, Agisoft
299 with GCPs, Agisoft without GCPs). The coordinates (easting (x), northing (y)) of the GCPs identified
300 within the georectified images from all three methodologies were evaluated against the Leica D-
301 GNSS RTK measured reference (considered ‘truth’) GCP coordinates using a suite of standard
302 statistical parameters (Equations 1 to 11). These statistics are the residuals which describe the
303 directional distance between the measured and observed each GCP position in the x (Equation 1) and
304 y (Equation 2) direction, the absolute residual which describes the non-directional distance between
305 the measured and observed each GCP position in the x (Equation 3) and y direction (Equation 4), the
306 mean bias which describes the mean residual in the x (Equation 5) and y direction (Equation 6), the
307 standard deviation which describes the spread of the differences in the x (Equation 7) and y positions
308 (Equation 8), the root mean squared difference (RMSD) which measures the difference between the
309 reference value and the observed values in the x (Equation 9) and y (Equation 10) directions, the
310 mean Euclidean distance ($Mean |(x, y)|$) which examines the mean horizontal distance between the
311 observed and measured x,y GCP positions (Equation 11) and the distance root mean squared
312 difference (DRMSD) (Equation 12) which expresses 2D precision by combining the x and y direction
313 standard deviations.

314

$$315 \quad \text{Residual, } x \text{ direction} = \Delta x = x_{\text{measured}} - x_{\text{observed}} \quad (1)$$

$$316 \quad \text{Residual, } y \text{ direction} = \Delta y = y_{\text{measured}} - y_{\text{observed}} \quad (2)$$

$$317 \quad \text{Absolute Residual, } x \text{ direction} = |\Delta x| = |x_{\text{measured}} - x_{\text{observed}}| \quad (3)$$

$$318 \quad \text{Absolute Residual, } y \text{ direction} = |\Delta y| = |y_{\text{measured}} - y_{\text{observed}}| \quad (4)$$

$$319 \quad \text{Mean Bias, } x \text{ direction} = \frac{1}{n} \sum \Delta x \quad (5)$$

$$320 \quad \text{Mean Bias, } y \text{ direction} = \frac{1}{n} \sum \Delta y \quad (6)$$

$$321 \quad \text{Std, } x \text{ direction} = \sigma_x = \sqrt{\frac{1}{n} \sum (\Delta x - \mu)^2} \quad (7)$$

$$322 \quad \text{Std, } y \text{ direction} = \sigma_y = \sqrt{\frac{1}{n} \sum (\Delta y - \mu)^2} \quad (8)$$

$$323 \quad \text{RMSD}_x = \sqrt{\frac{\sum (\Delta x)^2}{n}} \quad (9)$$

$$324 \quad \text{RMSD}_y = \sqrt{\frac{\sum (\Delta y)^2}{n}} \quad (10)$$

$$325 \quad \text{Mean Euclidean Distance} = \text{Mean } |(x, y)| = \frac{1}{n} \sum \sqrt{\Delta x^2 + \Delta y^2} \quad (11)$$

$$326 \quad \text{DRMSD} = \sqrt{\sigma_x^2 + \sigma_y^2} \quad (12)$$

327

328 2.7 Drone on-board sensor position and orientation data accuracy assessment

329 When high-accuracy GCPs (e.g. measured using an RTK GPS kit) are used in the Agisoft
 330 Metashape workflow, the software uses these to provide estimates of the ‘true’ position and
 331 orientation of the camera for each image. Using these estimates, the performance of the drone on-
 332 board sensor determined position was evaluated by comparing the drone position and orientation
 333 information for each image recorded by the drone on-board sensor to the reference position and
 334 orientation information produced by Agisoft Metashape. These values were evaluated visually using

335 box plots for each flight (Figure 5) and used to calculate field-derived bias (Equation 5) and RMSD
336 (Equation 9) values for each flight parameter (easting, northing, altitude, roll, pitch, yaw) for all
337 flights combined. The latter bias and RMSD values are required for the ensemble uncertainty analysis
338 presented in sections 2.8 and 3.2.

339 2.8 Spatial uncertainty ensemble analysis

340 An ensemble analysis is a methodology whereby the multiple simulations (e.g. ensemble
341 runs) with differing input parameters are statistically compared to determine the influence of varying
342 the input parameters. The following section describes an ensemble analysis conducted to evaluate the
343 combined impact of the field-derived uncertainty estimates for the drone position and orientation
344 parameters (obtained in section 2.7) on spatial accuracy within directly georectified images.

345 A pixel-wise grid (5472 x 3648 pixels) of horizontal and vertical field-of-view angles was
346 created by linearly interpolating between the edge values for the horizontal (-32.47° = left edge,
347 $+32.47^\circ$ = right edge) and vertical (-25.515° = top edge, $+25.515^\circ$ = bottom edge) field-of-view of the
348 DJI M2P camera. The position of each pixel was calculated using the direct ray tracing equations
349 described in section 2.4.4 for four synthetic flight scenarios with the camera at an altitude of 10 m and
350 25 m and at an angle of 0° (nadir) and 30° . For all cases the camera was positioned at the origin (i.e. x
351 (easting) = y (northing) = 0), facing due north (yaw = 0°) with a camera roll of 0° . These grids of x
352 and y position for each pixel represent the perfect case for a georectified image (i.e. uncertainty of
353 zero for all the flight parameters recorded by the drone).

354 Each ensemble run consisted of perturbing the flight parameter inputs of the ray vector
355 mathematical equations used to determine pixel position. For each of the four synthetic flight
356 scenarios a set of ($n = 50$) of flight parameter sets (easting, northing, altitude, roll, pitch yaw) were
357 created in which the values for each parameter included additive 'noise'. The noise for each data point
358 was created by randomly selecting points from a normally distributed synthetic noise dataset (standard
359 deviation equal to the RMSD, mean equal to the bias) using the field derived RMSD and bias
360 estimates for each flight parameter obtained in section 2.7.

361 For each set of flight parameters, the position (x,y) for each image pixel was calculated using
362 the direct ray tracing equations described in section 2.1. The absolute residual ($|\Delta x|$ and $|\Delta y|$)
363 between the target and ensemble pixel position grids was calculated and combined into a single value
364 by calculating the magnitude of the vector, from which the mean (e.g. the mean $|x, y|$, Equation 11),
365 and standard deviation was taken. The results are presented as contour plots of positional uncertainty
366 (m) and standard deviation for each of the flying height and camera angle combinations.

367 The workflow described here for generating maps of within image spatial uncertainty was
368 applied using custom Python scripts which are available from <https://github.com/JamieLab/SArONG>).

369 2.9 Application in an estuarine environment

370 A set of drone images were collected using a DJI M2P over the shoreline, including a quay
371 wall, and open water in an estuarine environment in Restronguet Creek, Cornwall, UK (50.196 °N, -
372 5.0636 °W). Data collection was planned to eliminate the issue of sun glint by avoiding flying at solar
373 noon and selecting a zenith angle when over water that was 90 degrees to the sun, as recommended in
374 (Duffy et al., 2018) as well as manually checking for sun glint artefacts in camera view in the field.
375 The images were georectified using the workflow described in section 2.4.1. The accuracy of the
376 georectified images was evaluated using set of five targets placed on the shore. The easting (m),
377 northing (m) and elevation (m) of the centre of each target was measured using the Leica GS-08 plus
378 D-GNSS RTK survey system and measurements were also taken at 1 metre spacing along the bottom
379 edge of the quay wall.

380 3 Results

381 3.1 Georectified image accuracy assessment

382 3.1.1. Average horizontal accuracy

383 The horizontal (x,y) accuracy of each georectification method is compared using a range of
384 statistical parameters (as presented in Tables 1 and 2). Mean $|x,y|$ is used within the text as it describes
385 the absolute mean distance between the observed (e.g. image extracted) and RTK-GNSS measured
386 GCP positions in the horizontal plane. Across all flying heights and camera angles, the presented
387 direct-georectification workflow is capable of georectifying image datasets with an average horizontal

388 accuracy consistent with the Agisoft Metashape approach without GCPs, which has a maximum
389 $Mean |(x, y)|$ of 4.32 m, but the accuracy is clearly lower than the Agisoft approach that uses GCPs,
390 which has a maximum $Mean |(x, y)|$ of 0.15 m. Figure 3 and the values presented in Tables 1 and 2
391 show a clear relationship between the average horizontal georectification accuracy of the individual
392 images (Python direct-georectification method) and Agisoft Metashape (without GCPs) with
393 increasing flying height or camera angle. At a flying height of 10 m the Python direct-georectification
394 was capable of georectifying the set images with an average horizontal accuracy ($Mean |x, y|$) of
395 0.94 m (Dataset A) to 1.09 m (Dataset B) when the camera angle was at nadir (0°) and 0.8 (Dataset A)
396 to 1.19 m (Dataset B) when the camera angle was 30° . At a flying height of 25 m, average horizontal
397 accuracy was 0.94 m (Dataset A) to 2.24 m (Dataset B) when the camera was at nadir and 2.63 m
398 (Dataset A) to 3.14 m (Dataset B) at 30° .

399 The spread of the differences in x, y positions of the identified GCPs (as shown by the
400 whisker plots in Figure 3 and the standard deviation values in Tables 1 and 2) also increases with
401 increasing altitude and camera angle. The differences in the statistics for the east and north directions
402 are likely for two potential reasons, firstly due to variability in the satellite constellation at the time of
403 observation and secondly because the impact of uncertainties in other flight parameters (roll, pitch,
404 yaw) will not have an equal impact in the easting and northing directions.

405

406

407

408

409

410

411

412

413 **Table 1.** Statistical description of the difference in the horizontal position of GCPs identified in
 414 images georectified using the Python workflow, Agisoft Metashape without GCPs and Agisoft
 415 Metashape with GCPs compared to the Leica D-GNSS RTK measured GCP locations for Dataset A.
 416 All statistics are calculated for the absolute residual in easting (Δx , Equation 3) and northing (Δy ,
 417 Equation 4), except bias which uses the residual (Equations 5 and 6). The range refers to the
 418 maximum absolute residual minus the minimum absolute residual.

Flight	Wind Dir ($^{\circ}$) (median + std)	Wind Speed (m s^{-1}) (median + std)	No. sats	Statistical Parameter	Python Method (without GCPs)		Agisoft Metashape (without GCPs)		Agisoft Metashape (with GCPs)	
					East	North	East	North	East	North
10 m, 0 $^{\circ}$	261 \pm 13	2.8 \pm 0.74	16	Range (m)	2.19	2.19	2.72	3.77	0.11	0.11
				Mean bias (m)	0.88	0.34	2.68	1.03	0.06	0.03
				Median	0.86	0.30	2.68	1.03	0.06	0.02
				Std (σ)	0.48	0.21	1.07	0.64	0.04	0.02
				RMSD	1.00	0.40	2.89	1.21	0.08	0.04
				Mean (x,y) (m)	0.94		2.87		0.07	
				DRMSD	0.53		1.25		0.05	
				Range (m)	1.61	1.61	5.30	5.78	0.12	0.12
10 m, 30 $^{\circ}$	301 \pm 8	4.1 \pm 0.9	19	Mean bias (m)	0.48	0.65	3.53	1.14	0.04	0.08
				Median	0.42	0.63	3.41	0.93	0.02	0.04
				Std (σ)	0.32	0.31	1.51	0.68	0.04	0.06
				RMSD	0.58	0.72	3.84	1.33	0.06	0.10
				Mean (x,y) (m)	0.80		3.71		0.09	
				DRMSD	0.45		1.66		0.07	
				Range (m)	1.74	1.74	1.62	2.36	0.05	0.05
				Mean bias (m)	0.50	0.80	1.58	0.60	0.02	0.01
25 m, 0 $^{\circ}$	258 \pm 7	4.0 \pm 0.3	17	Median	0.46	0.74	1.61	0.58	0.02	0.01
				Std (σ)	0.34	0.52	0.46	0.38	0.01	0.01
				RMSD	0.60	0.96	1.64	0.71	0.02	0.02
				Mean (x,y) (m)	0.94		1.69		0.02	
				DRMSD	0.62		0.60		0.02	
				Range (m)	5.57	5.57	2.57	1.86	0.41	0.41
				Mean bias (m)	1.75	1.96	1.18	2.63	0.08	0.13
				Median	1.66	1.89	1.12	2.67	0.06	0.09
25 m, 30 $^{\circ}$	323 \pm 7	6.0 \pm 1.1	19	Std (σ)	1.05	1.01	0.73	0.95	0.08	0.14
				RMSD	2.04	2.20	1.38	2.80	0.11	0.19
				Mean (x,y) (m)	2.63		2.88		0.15	
				DRMSD	1.46		1.20		0.16	

419

420

421 **Table 2.** Statistical description of the difference in the horizontal position of GCPs identified in
 422 images georectified using the Python workflow, Agisoft Metashape without GCPs and Agisoft
 423 Metashape with GCPs compared to the Leica D-GNSS RTK measured GCP locations for Dataset B.
 424 All statistics are calculated for the absolute residual in easting (Δx , Equation 3) and northing (Δy ,
 425 Equation 4), except bias which uses the residual (Equations 5 and 6). The range refers to the
 426 maximum absolute residual minus the minimum absolute residual.

Flight	Wind Dir (median + std)	Wind Speed (median + std)	No. sats	Statistical Parameter	Python Method (without GCPs)		Agisoft Metashape (without GCPs)		Agisoft Metashape (with GCPs)	
					East	North	East	North	East	North
10 m, 0°	308 ± 5	2.4 ± 0.41	17	Range (m)	1.39	1.26	0.46	1.24	0.03	0.03
				Mean bias (m)	0.62	0.90	2.69	2.13	0.02	0.01
				Median	0.60	0.90	2.69	2.13	0.02	0.01
				Std (σ)	0.42	0.35	0.20	0.33	0.01	0.01
				RMSD	0.75	0.96	2.70	2.15	0.02	0.01
				Mean (x,y) (m)	1.09		3.43		0.02	
				DRMSD	0.55		0.39		0.01	
				Range (m)	1.90	1.91	1.49	0.50	0.13	0.12
10 m, 30°	305 ± 4	2.4 ± 0.46	17	Mean bias (m)	0.92	0.75	1.71	2.99	0.03	0.07
				Median	0.94	0.67	1.74	3.07	0.02	0.05
				Std (σ)	0.44	0.51	0.47	0.53	0.03	0.04
				RMSD	1.02	0.90	1.77	3.04	0.04	0.08
				Mean (x,y) (m)	1.19		3.44		0.07	
				DRMSD	0.67		0.71		0.05	
				Range (m)	4.62	4.62	5.89	6.46	0.13	0.13
				Mean bias (m)	1.82	1.57	3.35	2.60	0.02	0.03
25 m, 0°	310 ± 4	4.2 ± 0.18	17	Median	1.64	1.30	3.29	2.59	0.01	0.02
				Std (σ)	1.13	1.13	1.57	1.65	0.03	0.03
				RMSD	2.14	1.94	3.70	3.08	0.03	0.04
				Mean (x,y) (m)	2.4		4.24		0.04	
				DRMSD	1.60		2.28		0.04	
				Range (m)	3.15	3.31	3.49	2.65	0.37	0.36
				Mean bias (m)	1.51	2.75	2.19	3.72	0.07	0.12
				Median	1.49	2.99	2.32	3.85	0.04	0.06
25, 30°	320 ± 5	5.1 ± 0.35	18/ 19	Std (σ)	0.62	1.32	1.05	1.67	0.08	0.14
				RMSD	1.64	3.05	2.43	4.08	0.11	0.18
				Mean (x,y) (m)	3.14		4.32		0.14	
				DRMSD	1.46		1.97		0.16	

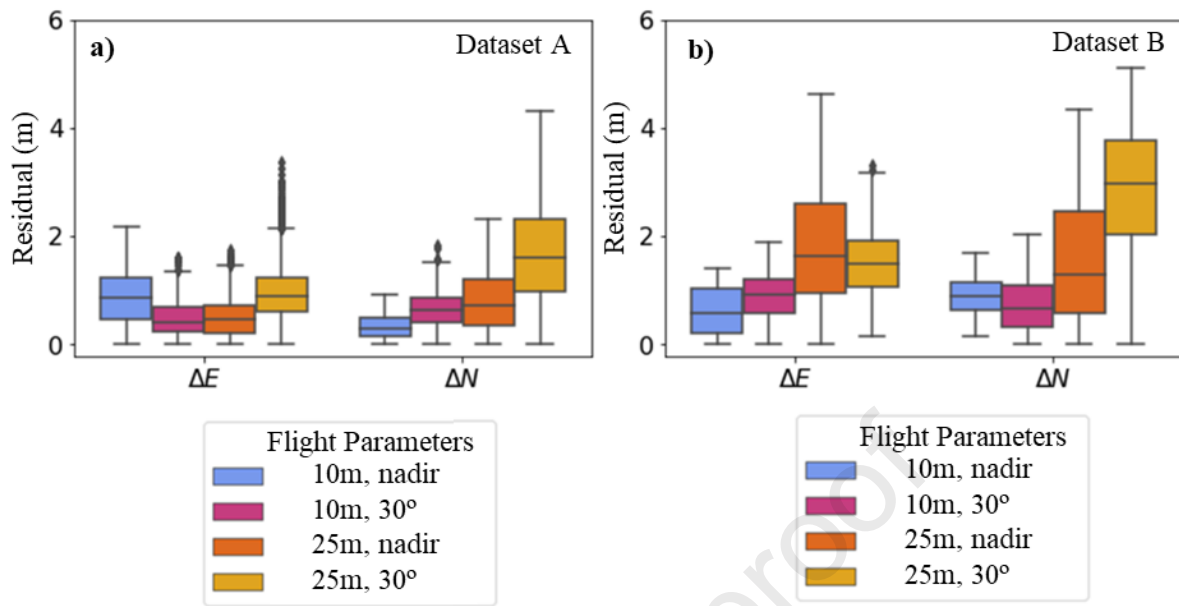


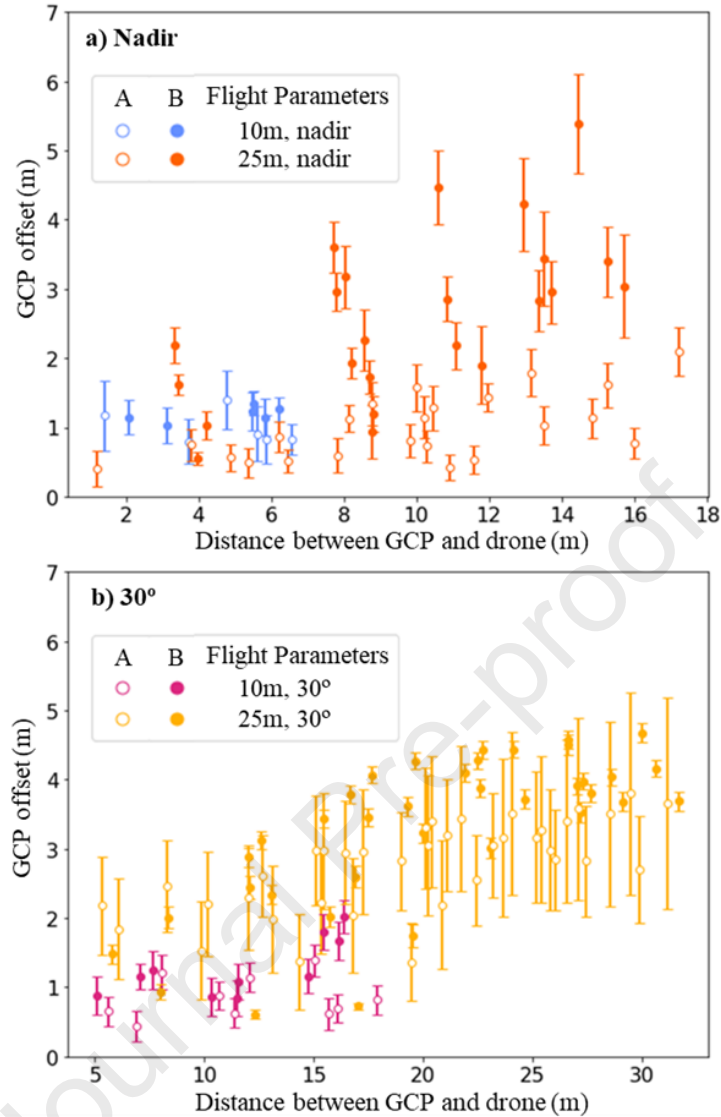
Figure 3. Distribution of absolute residual in easting (ΔE) and northing (ΔN) in metres (m) between the GCP position measured by the Leica D-GNSS RTK and observed in the direct-georectified images for all four drone flights at flying height of 10 and 25 metres above ground level (AGL) with the camera at nadir and 30° for Dataset A (Figure 3a) and Dataset B (Figure 3b).

428 3.1.2. Spatial variability in horizontal accuracy

429 To examine how accuracy varies spatially within each directly-georectified image, the distance
 430 between the measured and observed GCP positions (*mean* $|x, y|$, Equation 11), henceforth referred to
 431 as GCP accuracy, are calculated and plotted as a function of the distance between the drone and GCP
 432 (Figures 4a and 4b). In the images collected at 10 m with the camera angle at nadir there is low spatial
 433 variability in GCP accuracy (< 0.2 m), indicating that there is no strong relationship with distance
 434 from the drone at this elevation. Within the images collected at 25 m with the camera at nadir, GCP
 435 accuracy decreases with increasing distance from the drone by 1–1.5 m (over a distance of ~17
 436 metres). The results for Dataset A at 25 m (open yellow symbols, Figure 4b) exhibit high variability in
 437 accuracy for each individual GCP, as shown by the large error bars. The wind speed values shown in
 438 Table 1 and the wind-speed box plots in the Figure S1 (supporting materials) suggests that the

439 variance of wind speed values during this flight was relatively high (as indicated by a standard
440 deviation of 1.1 ms^{-1} , and a wind speed range of 3.5 ms^{-1} up to 8.2 ms^{-1}) indicating that gusting wind
441 may have been impacting drone stability during this hover flight. The results for Dataset B at 25 m
442 with the camera at nadir (filled orange symbols, Figure 4a) exhibit a large decrease in accuracy (up to
443 6 m) with increasing distance from the drone, which is likely due to an error in the recorded drone
444 heading (yaw) – see discussion in section 3.2.

445 There is an increase in spatial variability in GCP accuracy in the georectified images collected
446 with the camera angle at 30° and with increasing altitude. In images captured at 10 metres above
447 ground level with the camera at 30° the GCP accuracy decreases as distance from the drone increases
448 by 0.5 – 1 m over a distance of ~ 17 metres. While in images captured at 25 m above ground level
449 with the camera at 30 degrees GCP accuracy decreases with increasing distance from the sensor by up
450 to 4 m over a distance of ~ 30 metres.



451

452 **Figure 4.** The mean (scatter points) \pm std (error bars) in absolute residual from the GCP centre-point
 453 observed in the direct-georectified images and the Leica D-GNSS RTK GCP measurements as a
 454 function of the absolute distance of the GCP from the viewing position of the drone for all four drone
 455 flights at flying height of 10 and 25 metres above ground level with the camera at nadir (Figure 4a)
 456 and 30° (Figure 4b).

457 3.2 Drone on-board sensor position and orientation data accuracy assessment

458 For each of the flying heights and camera angles, the distribution of the differences in the
 459 position and orientation recorded for each image by the drone sensor and the reference values
 460 estimated by Agisoft Metashape are shown in Figure 5. In Dataset A, the difference between the
 461 reference eastings and northings for each image and the on-board sensor information are similar
 462 across all georectification methods. Residuals for both methods without ground control range between

463 0.5 – 2 metres. In Dataset B, easting is consistently < 1 metre, while variability in northing is higher
464 and ranges between 1 to 3 m throughout the four hover-flights.

465 The largest differences between the on-board record and reference drone information occur in
466 the yaw and roll values for the 25 m, nadir hover flight in Dataset B. In particular, the erroneous yaw
467 value (-12 to -19°) caused significant rotation of the entire field-of-view and resulted in a horizontal
468 offset in GCP position that increases with distance from the drone. In all the remaining hover flights
469 (Dataset A and B) the reference and observed camera orientation values (yaw, pitch, and roll) are
470 consistently between $\pm 0 - 5^\circ$.

471 The results show that error in position and orientation information can vary within a single
472 drone mission, suggesting that errors are not consistent in both time and space. It is unclear if this
473 variability was caused by a sudden change in environmental conditions (e.g. changes in wind-speed
474 and direction) or internal sensor variability. Except for the 25 m, 30° flight in Dataset A, no clear
475 relationship between environmental conditions (e.g. wind speed, wind direction, wind direction
476 relative to drone heading) and the accuracy of drone position and/or orientation as recorded by the on-
477 board sensor were identified in either Dataset A or B (see supporting information Text S4, Figure S1).

478 Datasets A and B were also combined to calculate a single mean bias (Equation 2) and RMSD
479 (Equation 6) value for each flight parameter: Easting (0.30 m, 1.00 m), Northing (0.32 m, 1.06 m),
480 Altitude (0.28 m, 0.36 m), Roll (2.01° , 2.48°), Pitch (-1.54° , 1.79°) and Yaw (1.77° , 2.86°). These
481 field-derived parameters are used to drive the uncertainty analysis described in section 2.5 to
482 understand individual pixel or within camera-view uncertainties, the results of which are presented in
483 section 3.3.

484

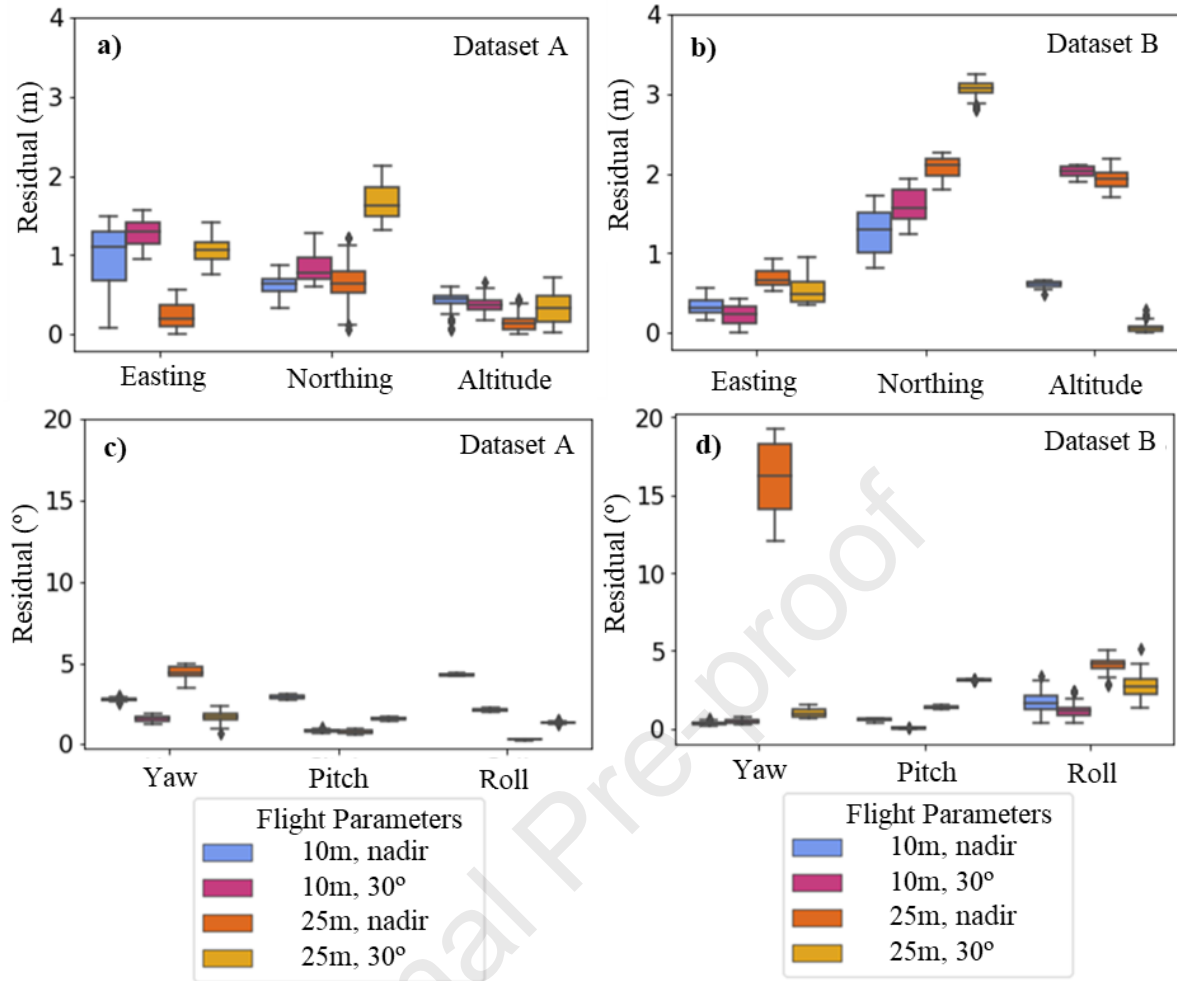


Figure 5. Absolute residual between the position (easting, northing, altitude) and orientation (yaw, pitch, roll) of the drone recorded by the on-board sensors and the Agisoft Metashape reference dataset. All four drone flights are shown (flying heights of 10 and 25 metres above ground level, camera angles of nadir and 30°) for Dataset A (Figures 5a, 5c) and Dataset B (Figures 5b, 5d).

485 3.3 Spatial uncertainty ensemble analysis

486 Figure 6 presents the results of the ensemble analysis showing spatially varying mean uncertainty (m)
 487 (left panels) and standard deviation (m) (right panels) for all sensor altitude (10 m, 25 m) and camera
 488 angle (nadir, 30°) combinations. Mean uncertainty in pixel position refers to the
 489 $Mean |(x, y)|$ (Equation 11) which describes the horizontal distance between the reference pixel
 490 positions (x,y) and the pixel positions (x,y) calculated in each ensemble run. At 10 m with the camera
 491 at 0° uncertainty in pixel position varies by 0.3 m, with a maximum difference of 1.6 ± 0.84 m (mean
 492 \pm std), increasing to a within image variation of 1.2 metres, with a maximum difference of 2.4 ± 1.3 m

493 when the camera is at 30° . At 25 m, variability in uncertainty (e.g. the range) increases to 1 metre with
 494 the camera at nadir and 3.2 m at 30° . As flying height and camera angle increase, both the magnitude
 495 and standard deviation in the resultant geolocation uncertainties increase.

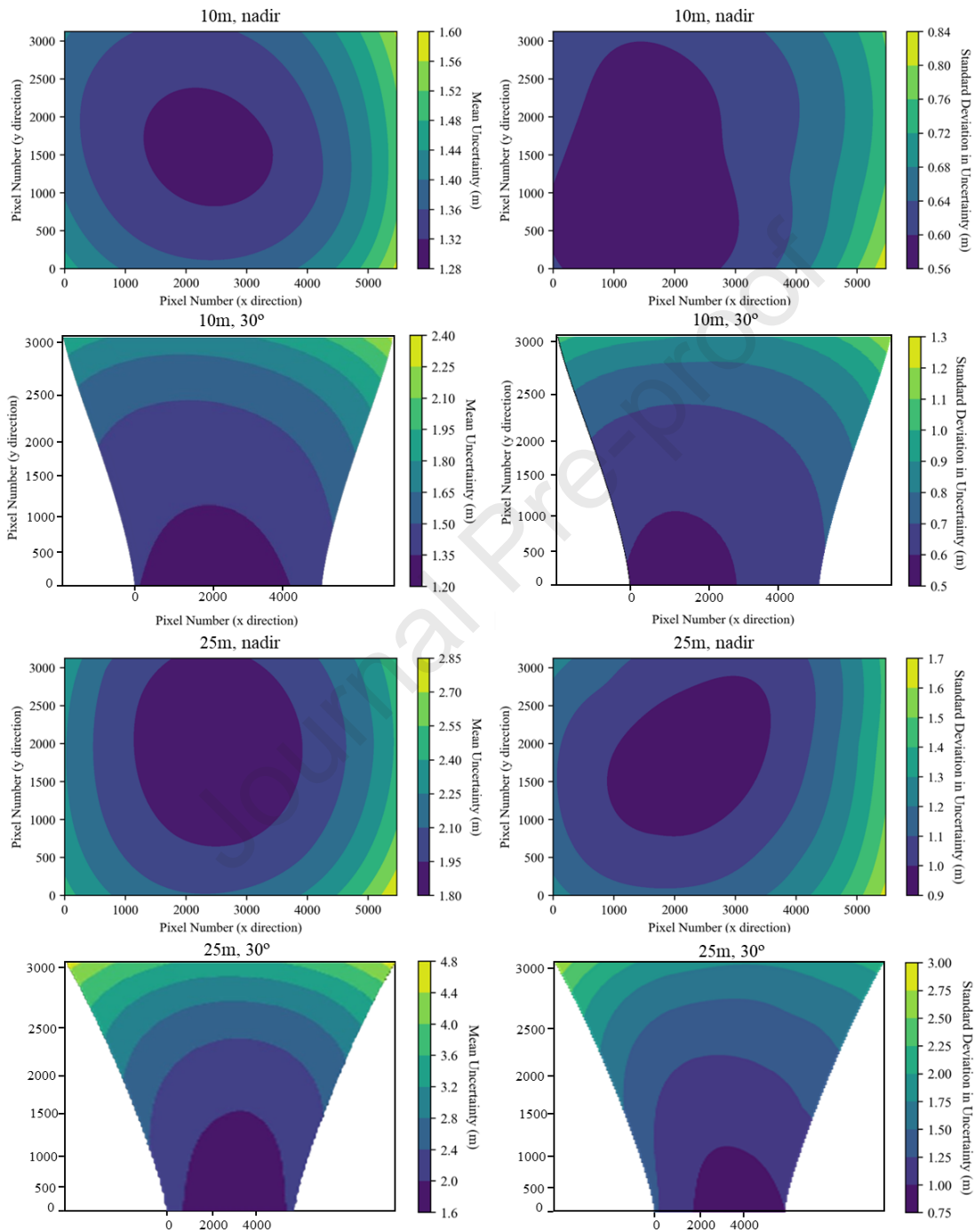


Figure 6. Spatially varying uncertainty grids of mean absolute difference in x, y position (in metres) (left hand panels) and standard deviation of the absolute difference in x,y position (in

metres) (right hand panels), in aerial images collected at heights of 25 m and 10 m with the sensor at nadir and 30°.

496 3.4 Application in an estuarine environment

497 Figure 7 demonstrates using the direct-georectification method on image data collected by a DJI M2P
 498 drone over an estuarine environment, where the shoreline and water offshore are visible. Table 3
 499 evaluates the differences between the measured (DGNSS) and image data provided (georectified
 500 images) position of a set of five GCPs deployed on the shore (Figure 7). The GCPs identified in the
 501 images taken at nadir at a height of 25 m had mean absolute difference in x,y position of 0.92 m
 502 increasing to 5.01 m when the camera is at 30°. These results are comparable to the field tests
 503 presented in section 3.1.1. (mean absolute difference in x,y position of 0.94 m at nadir increasing to
 504 2.9 m at 30°) and the uncertainty estimates presented in section 3.3 (mean absolute difference in x,y
 505 position of 1.9 m at nadir increasing to 3.2 m at 30°).

506 Overall, the values presented in Table 3 show that the spatial uncertainty for both the nadir
 507 and oblique camera angles at a flying height of 25 m are consistent to those identified in the field
 508 experiments shown in section 3.1.1 and 3.1.2 and the uncertainty assessment in section 3.3. It should
 509 be noted that as the GCPs are clustered in one area of the image they are not representative of all areas
 510 of the image, in particular for the 30° example due to the spatial variability in accuracy (i.e. as
 511 observed in section 3.1.2). However, they compared well to the results of the spatial uncertainty
 512 ensemble analysis presented in section 3.3.

Table 3. Comparison of measured GCP locations (D-GNSS RTK) and observed GCP locations in the Python direct-georectified images taken over Restronguet Creek.

Statistical Parameter	25 m, nadir		25 m, 30°	
	Δ East	Δ North	Δ East	Δ North
Range (m)	0.35	0.41	0.31	0.62
Bias (m)	0.20	0.88	3.96	3.06
Median (m)	0.24	0.90	3.85	2.88
Std (σ) (m)	0.15	0.15	0.62	0.46
RMSD (m)	0.25	0.90	4.01	3.09
Mean (x, y) (m)	0.92		5.01	
DRMSD (m)	0.21		0.24	

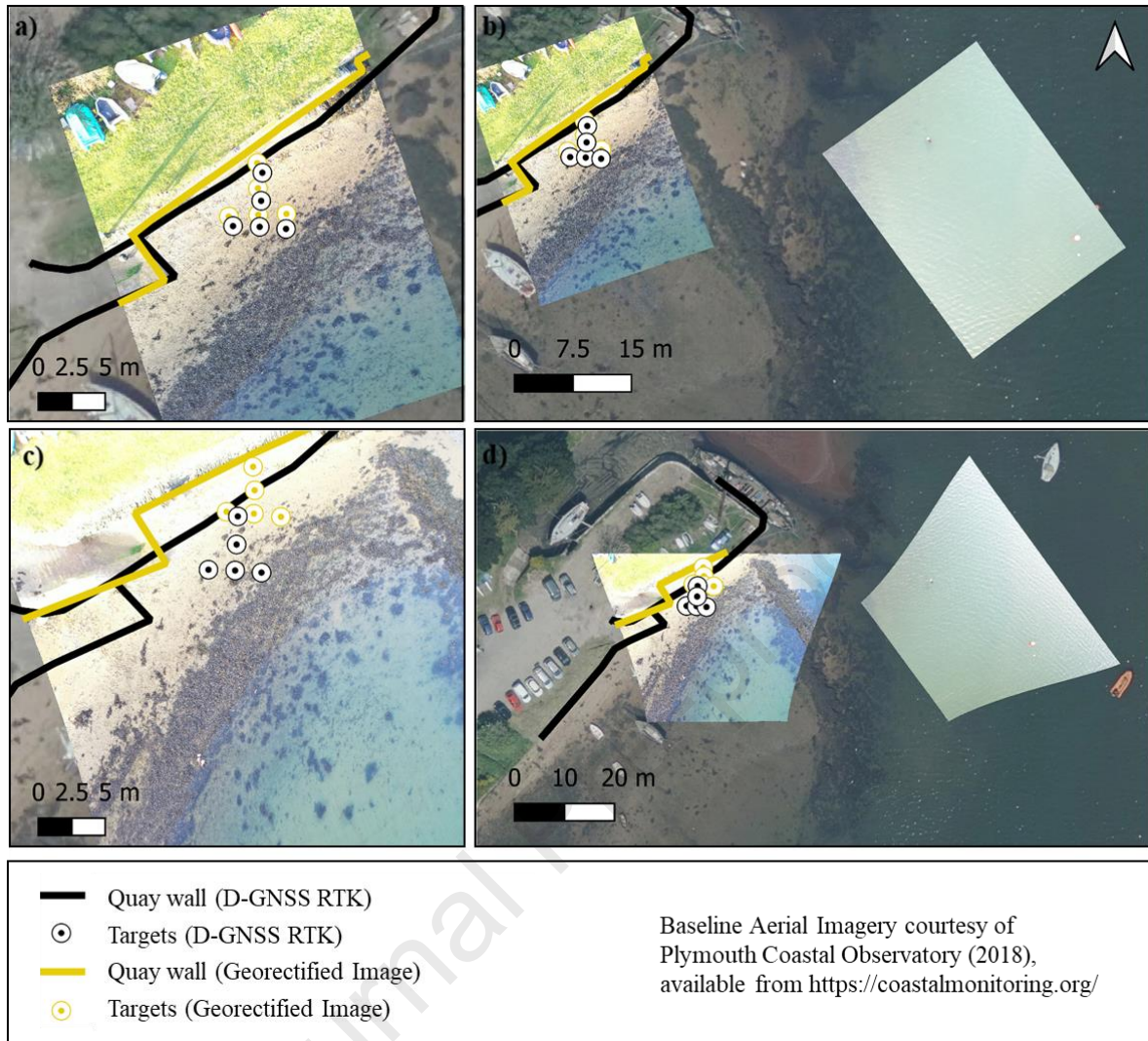


Figure 7. Images collected at an altitude of 25 m using a DJI M2P drone over an estuarine environment with a camera angle at nadir (Figures 4.7a, 4.7b) and 30° (Figures 4.7c, 4.7d) and directly-georectified using the presented python workflow. These are overlaid on a base layer of aerial image datasets collected by Plymouth Coastal Observatory and the position of the quay wall, and five targets placed on the foreshore, as measured using Leica D-GNSS RTK (shown in black) and visually identified in the georectified images (shown in yellow).

513 4 Discussion

514 We present a complete open-source workflow for direct-georectification of drone image data
515 which uses the drone position and orientation data to rectify the image. Field-tests show that, when
516 using the platform and sensor set-up described in this work, the methodology is capable of directly
517 georectifying image datasets with a consistent average horizontal accuracy < 2 m (research questions
518 1 and 2). This accuracy can decrease to 6 metres within a single image and its value is a function of
519 flying height and camera angle (research question 2). A relationship between increasing spatial
520 variability in horizontal accuracy and increasing altitude and camera angle was also observed. This
521 effect occurs as the impact of exterior camera angle errors increases with increasing viewing distance
522 from the drone to the ground (research question 3), which is a function of viewing angle and altitude.
523 This effect is clear in the results as at an altitude of 10 m the difference in average spatial accuracy of
524 georectified images taken at nadir or 30° is small and the within image spatial variability is low
525 (especially when compared to the 25 m examples).

526 Spatial variability of the geolocation uncertainties is important for quantitative data
527 applications as it not only describes how accurately the whole image is positioned on the ground but
528 also how accurately features within the image are represented (e.g. the dimensions or size of objects).
529 Easting, northing and yaw errors affect the geolocation accuracy of the image while roll, pitch and
530 altitude errors affect both the geolocation and the accuracy of feature representation. For the drone
531 platform used in this work (DJI Mavic 2 Pro) there are no published manufacturer specification
532 uncertainty estimates for the drone on-board sensor as this is proprietary information. However, this
533 work presents methods for characterising the uncertainty of the on-board sensors under field
534 conditions. Using these values to run an ensemble analysis then provides a means to estimate direct-
535 georectification accuracy without the use of ground control points. For the 25 m height, oblique (30°)
536 camera angle example these results can be directly compared to those presented in Schweitzer &
537 Cowen (2022) which presents a similar analysis but using uncertainty estimates for camera orientation
538 parameters based on manufacturer specifications of a typical IMU system. Comparing these results,
539 the spatial pattern of uncertainty is consistent between the two studies but the maximum positional

540 uncertainty when using field-derived uncertainty estimates (i.e. instead of manufacturer provided IMU
541 specifications) is higher by a factor of two.

542 4.1 Direct-georectification method limitations and uncertainties

543 It should be noted that the presented methodology is only suitable for use over low-relief
544 landscapes (e.g. such as relatively flat (water) surfaces) as the corner point ray-tracing will be less
545 effective when there are topographical features (e.g. within a river system with steep gradients). While
546 the field-site used in this work was low relief it was not a completely horizontal plane. The range and
547 standard deviation in GCP elevation in the camera field-of-view for each dataset, flying height and
548 camera angle is presented in Table S4 in the supporting materials. These show a clear increase in the
549 GCP elevation variability with increasing camera altitude and angle (due to the increased size of the
550 field-of-view). A simple calculation for a GCP at the furthest edge of an image taken with a maximum
551 difference in GCP elevation determined for each field-of-view (Table S4, supporting materials)
552 returns a maximum horizontal (both x and y direction) of ± 0.3 metres for the 10 m, 0° example
553 (smallest field-of-view) and ± 1.15 metres for the 25 m, 30° example. It is therefore likely that these
554 effects are reduced by averaging in the results presented in section 3.1.1 but are contributing to the
555 spatial variability observed in section 3.1.2. However, while variations in topography (e.g. the field-
556 site not being a completely horizontal surface) influence the results for accuracy presented in section
557 3.1, the relationship between flying height, camera angle and their uncertainties does not change. In
558 particular this relationship can be observed in the synthetic ensemble run results given in section 3.3
559 which are driven by drone sensor uncertainty estimates which are independent of flying height,
560 camera angle and the impact of field-site topography.

561 A notable contribution to the uncertainty evaluated in these results is the temporarily incorrect
562 yaw values (up to 20°) recorded during a sub-section of the Dataset B flight. Common causes of yaw
563 errors are poor compass calibration or magnetic interference (e.g. due to proximity to metal objects).
564 On this occasion, the compass was calibrated (e.g. on stable ground, away from metal objects) prior to
565 flying, and during the flight the DJI operating software did not flag any magnetic interference.
566 Furthermore, the compass recorded yaw with an accuracy of $1-2^\circ$ in subsequent hover flights within
567 the same drone mission. While the cause of this temporary yaw error has not been determined,

568 recommendations as to how to reduce yaw error both during missions and in image post-processing
569 can be made. One recommendation is to undertake a period of stable flight at the beginning of any
570 drone mission at a sufficient distance from metal objects (> 10 metres). A second recommendation is
571 to undertake a period of stable flight collecting an image dataset over a feature of known orientation
572 (e.g. the compass heading of the launch vessel) at the beginning and end of the drone mission. By
573 comparing this orientation to the orientation of the object as recorded in the drone images, it would be
574 possible to evaluate the accuracy of the drone on-board sensor and either use this as a quality control
575 procedure or apply corrections during post-processing. An alternative option for correcting and
576 quality controlling yaw data would be to identify the orientation of the main-axis of ocean glitter
577 within the camera field-of-view (an area of bright and sparkling reflection of the sun) as this will be a
578 function of sun azimuth and angle (Cox & Munk, 1956).

579 The uncertainty values presented in this work are based on a single drone and sensor set-up
580 (DJI M2P with in-built camera). While these uncertainty estimates are likely to be comparable to
581 other consumer-grade drones with the same on-board sensor set-up, independent accuracy testing may
582 be required for other platforms and sensor set-ups. It is recommended that accuracy testing should be
583 undertaken using multiple flights made over different days to capture the potential variability in
584 sensor accuracy caused by varying environmental conditions or unexplained drone sensor error (e.g.
585 as the flight compass errors observed in this work). The presented Python methodology and
586 subsequent analysis does not consider any offset between the drone sensors (inertial measurement
587 unit, GPS) and camera position. This source of uncertainty is instead included within the total
588 georectified image uncertainty. Sensor offsets could be determined via a boresight analysis (e.g. as
589 undertaken in Zhou, 2010). However, once boresight calibration has been undertaken, the camera
590 position must remain fixed for all subsequent flights which can reduce the agility of the system. It is
591 also important to note that different drone platforms will have different compass set-ups (e.g. some
592 have multiple compasses or use the IMU to provide yaw measurements). Determining the type of
593 compass observations being used will likely be important for understanding constraints on accuracy.

594 4.2 Potential applications in the coastal, estuarine and shelf sea environment

595 These results from this drone methodology and data collection have implications for other
596 low-altitude camera applications, for example cameras mounted on moving vessels at high-oblique
597 angles (e.g. angles $> \sim 45^\circ$ from nadir, angles which include the horizon) to collect images of sea
598 surface parameters such as white-capping (Callaghan et al., 2009; Norris et al., 2013; Woolf, 2005) or
599 sea-ice concentration (Butterworth & Miller, 2016; Hall et al., 2002). A simple calculation for a
600 camera mounted at 25 m and angled at 60° above nadir on a vessel with variations in the ships pitch
601 and roll of $\pm 2^\circ$ returns a maximum horizontal (x-direction) uncertainty of ± 1 m closest to the camera
602 increasing to ± 100 m furthest from the camera. To put this into context, if these small variations in
603 pitch and roll and not accounted for, an area of white capping or sea ice with a true length of 10
604 metres could appear to have a length of $\sim 9 - 10$ m close to the camera or $0 - 110$ m in the image
605 region furthest from the camera.

606 Due to the need to collect multiple images at single locations (and the variability of fine
607 temporal and spatial surface ocean parameters) these methods do not necessarily lend themselves to
608 quickly mapping large areas using image mosaicking approaches. However multiple observations
609 within scenes can be combined in post-processing to observe conditions across an area (rather than
610 viewing single isolated images). Potential applications of these methods include the observing or
611 mapping white capping, bubble or ocean glitter statistics and coverage which could be used to study
612 air-sea gas transfer (Bell et al., 2017; Woolf, 1993) studying mean-square slope of waves (Cox &
613 Munk, 1956), mapping the extent of suspended sediment plumes, the collection of spatially resolved
614 ocean colour data (Choo et al., 2022) for evaluating satellite observations, or the collection of fine
615 temporal and spatial resolution sea ice observations for shipping or biogeochemical studies. At a
616 capture height of 10 m and nadir camera angle images from the drone and camera systems evaluated
617 here, each image represents a region of $\sim 14 \times 9$ m corresponding to a single Sentinel 2 satellite pixel,
618 increasing to $\sim 30 \times 22$ m and approximately six Sentinel 2 pixels at a capture height of 25 m.
619 Therefore, the methods developed here could be used to provide data for evaluating data from
620 Sentinel 2, or other higher spatial resolution satellites, including characterising within satellite pixel
621 signal variability or mixing. Overall, spatially resolved observations of the ocean surface could

622 provide essential datasets to support satellite validation campaigns and to effectively bridge the gap
623 between spatially sparse in situ data and synoptic scale satellite observations.

624 5 Conclusions and recommendations

625 Low-cost drones are an agile platform for collecting high quality observations. However
626 established methods for accurately georectifying image datasets are impossible to apply over mobile
627 target surfaces that lack fixed points of reference (e.g. tie points and/or ground control points). This
628 study describes and evaluates an open-source method for georectifying aerial image datasets using
629 information provided by the on-board sensors within a commercially available lightweight drone
630 (referred to as direct-georectification). The results confirm that it is possible to use low-cost drone
631 sensors to accurately georectify drone image data collected over a water surface in the absence of
632 fixed points of reference when operating at low altitudes (< 25 m). Mean image accuracy decreases
633 and spatial variability in accuracy increases with increasing flight altitude and camera angle.

634 Estimates of spatial uncertainty within aerial image datasets are critical for determining the
635 usability of any extracted data. For example, determining which sections of the image can be used or
636 the size of features which that can be accurately identified.

637 Drones have the potential to be an effective tool for studying surface water processes,
638 comparing to in situ observations and/or characterising satellite observations. The experimental
639 techniques presented here will enable rapid collection of large quantities of high-quality image data,
640 accompanied by full uncertainty estimates.

641 **Acknowledgements**

642 This work is supported by a NERC PhD studentship (NE/L002434/1) as part of the GW4+ Doctoral
643 Training Program. The contribution of TB was supported by the NERC funded ORCHESTRA
644 (NE/N018095/1) and PICCOLO (NE/P021409/1) projects. This work was partially funded by the
645 ESA Scientific Assessment of Satellite Ocean Glitter (SArONG) (4000117644/16/NL/FF/gp) project
646 with some support from the Convex Seascape Survey. The authors would also like to thank I &
647 C.Rowlandson for use of their land in Blackwater, Cornwall, and the Watson family for use of their
648 Quay in Restronguet, Cornwall.

649 6 References

- 650 Almar, R., Bergsma, E. W. J., Catalan, P. A., Cienfuegos, R., Suarez, L., Lucero, F., Lerma, A. N.,
651 Desmazes, F., Perugini, E., Palmsten, M. L., & Chickadel, C. (2021). Sea state from single
652 optical images: A methodology to derive wind-generated ocean waves from cameras, drones and
653 satellites. *Remote Sensing*, *13*(4), 1–8. <https://doi.org/10.3390/rs13040679>
- 654 Andriolo, U., Garcia-Garin, O., Vighi, M., Borrell, A., & Gonçalves, G. (2022). Beached and Floating
655 Litter Surveys by Unmanned Aerial Vehicles: Operational Analogies and Differences. *Remote*
656 *Sensing*, *14*(6), 1–12. <https://doi.org/10.3390/rs14061336>
- 657 Bell, T. G., Landwehr, S., Miller, S. D., De Bruyn, W. J., Callaghan, A. H., Scanlon, B., Ward, B.,
658 Yang, M., & Saltzman, E. S. (2017). Estimation of bubble-mediated air-sea gas exchange from
659 concurrent DMS and CO₂ transfer velocities at intermediate-high wind speeds. *Atmospheric*
660 *Chemistry and Physics*, *17*(14), 9019–9033. <https://doi.org/10.5194/acp-17-9019-2017>
- 661 Butterworth, B. J., & Miller, S. D. (2016). Air-sea exchange of carbon dioxide in the Southern Ocean
662 and Antarctic marginal ice zone. *Geophysical Research Letters*, *43*(13), 7223–7230.
663 <https://doi.org/10.1002/2016GL069581>
- 664 Callaghan, A. H., White, M., Callaghan, A. H., & White, M. (2009). Automated Processing of Sea
665 Surface Images for the Determination of Whitecap Coverage. *Journal of Atmospheric and*
666 *Oceanic Technology*, *26*(2), 383–394. <https://doi.org/10.1175/2008JTECHO634.1>
- 667 Cassano, J. J., Seefeldt, M. W., Palo, S., Knuth, S. L., Bradley, A. C., Herrman, P. D., Kernebone, P.
668 A., & Logan, N. J. (2016). Observations of the atmosphere and surface state over Terra Nova
669 Bay, Antarctica, using unmanned aerial systems. *Earth System Science Data*, *8*(1), 115–126.
670 <https://doi.org/10.5194/essd-8-115-2016>
- 671 Cavanaugh, K. C., Cavanaugh, K. C., Bell, T. W., & Hockridge, E. G. (2021). An Automated Method
672 for Mapping Giant Kelp Canopy Dynamics from UAV. *Frontiers in Environmental Science*,
673 *8*(February), 1–16. <https://doi.org/10.3389/fenvs.2020.587354>
- 674 Choo, J., Cherukuru, N., Lehmann, E., Paget, M., Mujahid, A., Martin, P., & Müller, M. (2022).
675 Spatial and temporal dynamics of suspended sediment concentrations in coastal waters of the

- 676 South China Sea, off Sarawak, Borneo: ocean colour remote sensing observations and analysis.
677 *Biogeosciences*, 19(24), 5837–5857. <https://doi.org/10.5194/bg-19-5837-2022>
- 678 Cox, C., & Munk, W. (1956). Slopes of the sea surface deduced from photographs of sun glitter.
679 *Bulletin of the Scripps Institution of Oceanography*, 401–488.
- 680 Cunliffe, A., Tanski, G., Radosavljevic, B., Palmer, W., Sachs, T., Lantuit, H., Kerby, J., & Myers-
681 Smith, I. (2019). Rapid retreat of permafrost coastline observed with aerial drone
682 photogrammetry. *Cryosphere*, 13(5), 1513–1528. <https://doi.org/10.5194/tc-13-1513-2019>
- 683 Duffy, J. P., Cunliffe, A. M., DeBell, L., Sandbrook, C., Wich, S. A., Shutler, J. D., Myers-Smith, I.
684 H., Varela, M. R., & Anderson, K. (2018). Location, location, location: considerations when
685 using lightweight drones in challenging environments. *Remote Sensing in Ecology and*
686 *Conservation*, 4(1), 7–19. <https://doi.org/10.1002/rse2.58>
- 687 Duffy, J. P., Pratt, L., Anderson, K., Land, P. E., & Shutler, J. D. (2018). Spatial assessment of
688 intertidal seagrass meadows using optical imaging systems and a lightweight drone. *Estuarine,*
689 *Coastal and Shelf Science*, 200, 169–180. <https://doi.org/10.1016/J.ECSS.2017.11.001>
- 690 Ekaso, D., Nex, F., & Kerle, N. (2020). Accuracy assessment of real-time kinematics (RTK)
691 measurements on unmanned aerial vehicles (UAV) for direct geo-referencing. *Geo-Spatial*
692 *Information Science*, 23(2), 165–181. <https://doi.org/10.1080/10095020.2019.1710437>
- 693 Glassner, A. S. (1989). *An introduction to ray tracing*. Morgan Kaufmann.
- 694 Gray, P. C., Larsen, G. D., & Johnston, D. W. (2022). Drones address an observational blind spot for
695 biological oceanography. *Frontiers in Ecology and the Environment*, 20(7), 413–421.
696 <https://doi.org/10.1002/fee.2472>
- 697 Hall, R. J., Hughes, N., & Wadhams, P. (2002). A systematic method of obtaining ice concentration
698 measurements from ship-based observations. *Cold Regions Science and Technology*, 34(2), 97–
699 102. [https://doi.org/10.1016/S0165-232X\(01\)00057-X](https://doi.org/10.1016/S0165-232X(01)00057-X)
- 700 Jeziorska, J. (2019). UAS for wetland mapping and hydrological modeling. *Remote Sensing*, 11(17).
701 <https://doi.org/10.3390/rs11171997>

- 702 Johnston, D. W. (2019). Unoccupied aircraft systems in marine science and conservation. *Annual*
703 *Review of Marine Science*, 11, 439–463. <https://doi.org/10.1146/annurev-marine-010318->
704 095323
- 705 Kislik, C., Dronova, I., & Kelly, M. (2018). UAVs in support of algal bloom research: A review of
706 current applications and future opportunities. *Drones*, 2(4), 1–14.
707 <https://doi.org/10.3390/drones2040035>
- 708 Mallast, U., & Siebert, C. (2019). Combining continuous spatial and temporal scales for SGD
709 investigations using UAV-based thermal infrared measurements. *Hydrology and Earth System*
710 *Sciences*, 23(3), 1375–1392. <https://doi.org/10.5194/hess-23-1375-2019>
- 711 Norris, S. J., Brooks, I. M., Moat, B. I., Yelland, M. J., de Leeuw, G., Pascal, R. W., & Brooks, B.
712 (2013). Near-surface measurements of sea spray aerosol production over whitecaps in the open
713 ocean. *Ocean Science*, 9(1), 133–145. <https://doi.org/10.5194/os-9-133-2013>
- 714 Pucino, N., Kennedy, D. M., Carvalho, R. C., Allan, B., & Ierodiaconou, D. (2021). Citizen science
715 for monitoring seasonal-scale beach erosion and behaviour with aerial drones. *Scientific Reports*,
716 11(1), 1–17. <https://doi.org/10.1038/s41598-021-83477-6>
- 717 Schweitzer, S. A., & Cowen, E. A. (2022). A Method for Analysis of Spatial Uncertainty in Image
718 Based Surface Velocimetry. *Frontiers in Water*, 4(April), 1–11.
719 <https://doi.org/10.3389/frwa.2022.744278>
- 720 Seymour, A. C., Ridge, J. T., Rodriguez, A. B., Newton, E., Dale, J., & Johnston, D. W. (2018).
721 Deploying Fixed Wing Unoccupied Aerial Systems (UAS) for Coastal Morphology Assessment
722 and Management. *Journal of Coastal Research*, 34(3), 704–717.
723 <https://doi.org/10.2112/JCOASTRES-D-17-00088.1>
- 724 Shang, S., Lee, Z., Lin, G., Hu, C., Shi, L., Zhang, Y., Li, X., Wu, J., & Yan, J. (2017). Sensing an
725 intense phytoplankton bloom in the western Taiwan Strait from radiometric measurements on a
726 UAV. *Remote Sensing of Environment*, 198, 85–94. <https://doi.org/10.1016/j.rse.2017.05.036>
- 727 Ventura, D., Bonifazi, A., Gravina, M. F., Belluscio, A., & Ardizzone, G. (2018). Mapping and

- 728 classification of ecologically sensitive marine habitats using unmanned aerial vehicle (UAV)
729 imagery and Object-Based Image Analysis (OBIA). *Remote Sensing*, 10(9), 1–23.
730 <https://doi.org/10.3390/rs10091331>
- 731 Williamson, J. E., Duce, S., Joyce, K. E., & Raoult, V. (2021). Putting sea cucumbers on the map:
732 projected holothurian bioturbation rates on a coral reef scale. *Coral Reefs* 2021 40:2, 40(2),
733 559–569. <https://doi.org/10.1007/S00338-021-02057-2>
- 734 Woolf, D. K. (1993). Bubbles and the air-sea transfer velocity of gases. *Atmosphere - Ocean*, 31(4),
735 517–540. <https://doi.org/10.1080/07055900.1993.9649484>
- 736 Woolf, D. K. (2005). Parametrization of gas transfer velocities and sea-state-dependent wave
737 breaking. *Tellus, Series B: Chemical and Physical Meteorology*, 57(2), 87–94.
738 <https://doi.org/10.1111/j.1600-0889.2005.00139.x>
- 739 Zappa, C. J., Brown, S. M., Laxague, N. J. M., Dhakal, T., Harris, R. A., Farber, A. M., &
740 Subramaniam, A. (2020). Using Ship-Deployed High-Endurance Unmanned Aerial Vehicles for
741 the Study of Ocean Surface and Atmospheric Boundary Layer Processes. *Frontiers in Marine*
742 *Science*, 6(January), 1–17. <https://doi.org/10.3389/fmars.2019.00777>
- 743 Zhou, G. (2010). Geo-referencing of video flow from small low-cost civilian UAV. *IEEE*
744 *Transactions on Automation Science and Engineering*, 7(1), 156–166.
745 <https://doi.org/10.1109/TASE.2008.2010948>

746

747

Highlights

- We present an open-source workflow for georectifying drone image data
- It is capable of accuracies of ± 1 metre but is sensitive to viewing distance
- The method is suitable for use over water surfaces where there are no fixed points
- Potential uses include mapping whitecap fraction, ocean glitter and ocean color

Journal Pre-proof

Declaration of interests

The authors declare that they have no known competing financial interests or personal relationships that could have appeared to influence the work reported in this paper.

The authors declare the following financial interests/personal relationships which may be considered as potential competing interests:

Journal Pre-proof